Experimental characterization and modelling of UO2 behavior at high temperatures and high strain rates

Maxime Salvo, Sercombe Jérôme, Jean-Claude Ménard, Jérôme Julien, Thomas Helfer, Thierry Désoyer

Experimental characterization and modelling of UO_2 behaviour at high temperatures and high strain rates

Maxime Salvo[a], Jérôme Sercombe[a], Jean-Claude Ménard[b], Jérôme Julien[a], Thomas Helfer[a] and Thierry Désoyer[c]

[a] CEA, DEN, DEC/SESC, F-13108 Saint-Paul-lez-Durance, France.
[b] CEA, DEN, DEC/SPUA, F-13108 Saint-Paul-lez-Durance, France.
[c] CNRS, LMA, 13402 Marseille Cedex 20, France.

Abstract

This work presents an experimental characterization of uranium dioxide (UO_2) in compression under Reactivity Initiated Accident (RIA) conditions. Pellet samples were tested at four temperatures (1100, 1350, 1550 and 1700°C) and at a strain rate varying over 4 decades (10^{-4} - 10^{-3} - 10^{-2} - 10^{-1}/s). The experimental results show that the stress-strain curves cannot be fitted with a unique power law as it is the case at smaller strain rates ($10^{-9} - 10^{-5}$/s). A strain-hardening also appears in most of the tests. The microstructural observations show a pronounced evolution of the porosity at the pellet center during the tests. A hyperbolic sine model which accounts for volume variations (pore compressibility) was therefore proposed to describe the behaviour of UO_2 on a large range of temperatures (1100-1700°C) and strain rates (10^{-9}-10^{-1}/s). The Finite Element simulations of the compression tests lead to results (maximum stress, axial and hoop strain distribution, porosity distribution) in good agreement with the measurements. The model was then assessed on a database of more than two hundred creep tests.

Introduction

The Reactivity Initiated Accident (RIA) scenario postulates the ejection of a control rod bundle with a very fast increase of power in the neighbouring fuel rods (Energy deposition $\sim$ 100 cal/g UO_2 in 30-70 ms). In the 1990s, the use of Mixed OXide fuel (MOX) and of high burnup fuels in reactors led to the development of experimental programs to determine the impact of a RIA on these products [Fuketa et al., 2001, Schmitz and Papin, 1999, Papin et al., 2007].

The interpretation of RIA tests relies on the development of computer codes able to reproduce the thermomechanical behaviour of fuel rods during

the transient [Geelhood, 2010, Papin et al., 2007, Romano et al., 2006, Sercombe et al., 2010, Suzuki et al., 2006]. To improve the codes, it is essential to have behaviour models and failure criteria for the cladding [Cazalis et al., 2007] as well as for the fuel. The development of constitutive models for the fuel should be based on a laboratory characterization under appropriate conditions: temperature 1000-2700°C, strain rates up to 1/s.

The mechanical behaviour of UO_2 at high temperatures ($1000 - 2000°C$) has been extensively studied by creep experiments [Dherbey et al., 2002, Guérin, 1975, Monerie and Gatt, 2006, Radford and Terwilliger, 1975, Sauter and Leclercq, 2003, Seltzer et al., 1971]. Two creep deformation mechanisms have been identified depending on the stress and temperature level [Seltzer et al., 1971, Ashby, 1972] : diffusion creep and dislocation creep. These mechanisms are generally described by power-laws with Arrhenius temperature-dependent terms. Diffusion creep is dominant in the low stress-region. The strain rate varies linearly with the stress and is proportional to the reciprocal of the grain size squared. Dislocation creep is dominant at high stresses. The strain rate varies as stress to the power 3 to 8 and is generally independent of grain size. Recently, these creep mechanisms have been embedded in a three-dimensional macroscopic formulation where the volume variation of the material is taken into account [Monerie and Gatt, 2006].

Contrary to the low strain rate domain characterized by creep tests, little is known on the behaviour of uranium dioxide at high strain rates. The few experimental studies available show that the two creep deformation mechanisms are no longer adequate when the strain rates exceed 10^{-3}/s [Guérin, 1975, Roberts, 1974, Tachibana et al., 1976]. In this paper, the definition of a constitutive model for uranium dioxide suitable for a broad range of strain rates ($10^{-9} - 10^{-1}$/s) and temperatures ($1100 - 1700°C$) is presented. The results from a dedicated series of strain-rate controlled compression tests at high temperatures are first detailed. The evolution of the specimen microstructure is assessed by Scanning Electron Microscopy (SEM). Finite Element simulations of the strain-rate controlled tests and of more than 200 creep tests are then analyzed to assess the performance of the constitutive model.

1 Experiments

1.1 Characterization of test samples

The samples used in this study are commercial uranium dioxide sintered cylindrical pellets of approximately 8.2 mm in diameter (d_0) and 12 mm in

height (h_0). The sintering process ensured that the Oxygen/Uranium ratio was close to 2 (stoichiometry). Hydrostatic weighing in alcohol was used to estimate the relative density of the material (theoretical density 10.96 g/cm^3): 96.4% on average with a standard deviation of 0.3%.

Some samples were then sawed, the surfaces coated with an epoxy resin and polished prior to their observations by Scanning Electron Microscopy (SEM), see Figure 1. The polishing roughness is gradually decreased to 0.25 μm (diamond pastes) and there is a final step involving a colloidal solution of silica (0.04 μm). This careful polishing of the cross-section aims at limiting as much as possible the damage of the samples during the preparation.

From the SEM images, the average grain size was manually found close to 9 μm (calculated as the average of the grains situated on 4 intersecting lines). The commercial software ProAnalysis® was used to estimate the pore size distribution from the images. First, the grey images were reprocessed to generate binary images where pores appear white and the matrix black. By estimating the number of white pixels and the total number of pixels, the surface porosity of the material was assessed. The pore size distribution was obtained by converting each white zone into an equivalent disk with a specific diameter.

The surface porosity appeared fairly uniform in the samples. On average, it reached 5.2% with a standard deviation of 0.6%. Half of the pore volume was formed of pores with a diameter less than 3 μm. These fine pores were mostly located in the grains. The larger pores were in majority at the grain boundaries. The maximum pore size observed on the micrograph of Figure 1 is $\sim$30 μm, consistent with the maximum grain size. The statistics are based on six measures performed on two different samples. The observation area (500 μm by 750 μm) is important compared to the maximum grain and pore size ($\sim$ 30 μm).

1.2 Test matrix and procedure

The testing equipment is shown schematically in Figure 2. Mechanical tests on the fuel pellets have been performed with an Instron 1185 compression test machine with a maximum load capacity of 50 kN. The compression machine is equipped with an oven able to heat the fuel to a maximum temperature of 1800°C. The gas composition in the oven is controlled (95% Ar, 5% H_2) in order to prevent any stoichiometry change during the tests.

The focus of this work being strain rate effects, strain-rate driven tests have been carried out on the pellet samples. In the tests, the displacement rate of the cross head is kept constant until a final discharge. The tests were performed at four prescribed temperatures: 1100, 1350, 1550 and 1700°C.

At each temperature, four samples were tested with a displacement rate increased by decades from a minimum of 0.1 mm/min until a maximum of 100 mm/min (leading to a corresponding strain rates between 10^{-4}/s and 10^{-1}/s). Some of the tests were doubled or tripled to check the reproductibility.

The testing procedure reads as follows. First, the sample is placed between the two tungsten end-plates, see Figure 2, right. A small load not exceeding 250 N (5 MPa) is then applied. The gas composition in the oven is checked. The temperature is then increased manually until it reaches 200°C. This manual step is followed by a ramp at 20 °C/min until the prescribed temperature. These conditions are maintained 2 hours in order to guaranty a uniform temperature in the sample. The strain rate-driven loading sequence is then applied.

During the test, the speed of the cross-head is regulated and the contraction-elongation of the pellet is measured continuously by two extensometers in contact with the lower and upper Tungsten plates. From these measurements, the true strain ε_{zz} of the pellet is calculated according to equation 1 where the deformed height of the pellet is considered ($h = h_0 + \Delta h$ with Δh the variation in height). The axial stress σ_{zz} is estimated from the force F measured by the load cell and from the non-deformed diameter d_0 of the pellet, see equation 2. Significant friction occurs at pellet ends which makes section growth unlikely.

$$\varepsilon_{zz} = \ln\left(\frac{h}{h_0}\right) \tag{1}$$

$$\sigma_{zz} = -\frac{4F}{\pi d_0^2} \tag{2}$$

2 Test results

2.1 Stress-Strain curves

Figure 3 illustrates the (axial) stress-strain curves obtained at the strain rates 10^{-3}/s and 10^{-1}/s and at all the temperatures. The general tendency for a given strain rate is a decrease of the measured stress with temperature as expected in strain-rate driven tests [Guérin, 1975, Tachibana et al., 1976]. A strain hardening conversely proportional to the temperature, i.e., $d\sigma/d\varepsilon = f(1/T)$, is also apparent. In most of the tests, the axial strain reached 20% with no apparent damage of the samples. At 1100°C however, the tests were interrupted because of the development of axial cracks.

Figure 4 illustrates the (axial) stress-strain curves obtained at the two temperatures 1350 and 1700°C and at all the strain rates. The general tendency for a given temperature is an increase of the stress with the strain rate. A strain hardening increasing with the strain rate is also observed. This hardening is usually attributed to an increase of the sample diameter during the test [Guérin, 1975].

2.2 Macroscopic evolution

The importance of temperature and strain rate with respect to the samples' damage was clearly seen in these test series. Short axial cracks (1-3 mm long, see Figure 5) were observed on the pellets tested at 1350°C at the highest strain rates (10^{-2} and 10^{-1}/s) and on all the pellets tested at 1100°C. No damage was observed during the other tests: 1350°C and 10^{-4}-10^{-3}/s, 1550 and 1700°C. Due to friction at pellet ends, the samples showed a barrel shape with significant diameter increase at mid-height, see Figure 5. The post-test diameter of the pellets $d(z)$ was systematically measured at ten regularly spaced points along three generatrices. The hoop strain axial profile $\varepsilon_{\theta\theta}(z)$ was then estimated according to :

$$\varepsilon_{\theta\theta}(z) = \ln\left(\frac{d(z)}{d_0}\right) \tag{3}$$

A fit of the diameter axial profile with a quadratic function was then used to estimate the post-test average diameter of the pellet d_{av} and the volume variation $\Delta V/V$. Excellent correlation coefficients (> 0.99) were obtained when fitting the diameter axial profiles due to the nearly perfect symmetry of the deformation with respect to the mid-pellet plane. This indicates that the positioning of the sample and the parallelism of the upper and lower tungsten rods during the tests were correct.

In Figure 6, the maximum and average residual hoop strains (calculated from Equation 3 with the maximum and average diameters) are plotted in function of the residual axial strains. The latter are not identical in all the tests. At 1100°C, the tests were usually interrupted earlier to avoid dispersion of the samples after cracking. In most of the tests however, the residual axial strains exceeded 15%. The linear fit of the average hoop versus axial strains leads a correlation coefficient very close to 1 (0.9977). In theory, in an isotropic incompressible material subjected to a uniaxial compression, one should have $\varepsilon_{rr}/\varepsilon_{zz} = \varepsilon_{\theta\theta}/\varepsilon_{zz} = -0.5$. A small deviation from -0.5 is observed in Figure 6 since the slope of the linear regression equals -0.4784. This indicates that the volume of the samples decreased during the tests.

The relative density of the pellets was systematically measured by hydrostatic weighing in alcohol before and after the tests. Before testing, the average relative density was 96.4% with a standard deviation of 0.3%. The densities of the samples loaded at 1550 and 1700°C was found relatively independent of temperature and strain rate. On average, it was close to 97.4% with a standard deviation less than 0.1%. It indicates that the volume of the samples was significantly reduced ($\simeq 1\%$) during the tests. More scatter was found concerning the densities of the samples loaded at 1100 and 1350°C. No clear trend with the strain rate could be seen. However, the average densities were close to the initial density of the samples (96.4%) indicating that the volume had not been affected too much by the tests.

2.3 Microstructure evolution

SEM image analyses were performed on all the tested samples to study the evolution of the microstructure. The technique is described in Section 1.1. The samples were cut along the (r, z) plane. Three different locations were considered for SEM : the center of the pellet, the periphery of the pellet at mid-height, the upper extremity of the pellet. The evolution of the measured surface porosity with the strain rate is given in Figure 7 for all the temperatures.

The results show that the pore volume evolves differently during the test depending on the location. At the top of the pellet, the porosity appears fairly independent of the strain rate and of the temperature but presents a considerable scatter (3.5-4.8%). Most of the values are within twice the standard deviation (0.6%) associated with the pre-test porosity (average 5.2%).

At the periphery of the sample, the post-test porosity is fairly constant whatever the test conditions with an average value close to 3.9%. It indicates that some pore volume was lost during the thermal and loading sequences.

The microstructure of the pellet center is also modified during the tests. First, the measured surface porosities are always less than 4%. They also seem to increase with the strain rate. The evolution with temperature is less obvious. At 10^{-4}/s, the average porosity is equal to 2.4%. Slightly greater average values (2.8 - 3%) are obtained at the other strain rates. These results show that the porosity at the center of the specimen was considerably reduced during the tests (by 1 - 2%). The pore size distributions of Figure 8 confirm this evolution. Most of the pores in diameter greater than 4 μm disappeared during the tests at 1700°C. The evolution of the grain size is furthermore presented in Figure 9. Consistent with the pore evolution, a flattening of the grains apparently took place at the pellet center, but not at the pellet periphery and top extremity. The arrow on the right of Figure 9 gives the

compression axis and the direction in which the grain diameter has decreased.

These results show that the densification of the samples measured by hydrostatic weighing in alcohol is not homogeneous but preferentially occurred at the center of the pellet. As shown later, this is due to the non-homogeneous stress distribution in the pellet resulting from friction at pellet ends. It may be noticed that the grain boundaries were uncracked in spite of the high level of strain (20%) at the end of the tests. This is surprising since grain boundary cracking related to sliding at the grain interfaces has been observed after creep tests performed at similar temperatures and strain levels [Dherbey et al., 2002]. The lack of grain boundary fragmentation in our tests is certainly due to the accommodation of stresses by pore compression and grain plasticity. The samples tested by Dherbey et al. [Dherbey et al., 2002] were significantly denser than ours (relative density of more than 98%) and hence probably less prone to stress accomodation by pore compression.

2.4 Power-law fit

The strains of uranium dioxide during creep tests, bending tests or strain-rate driven tests are usually described by power laws of the following form:

$$\dot{\varepsilon} = K\sigma^n e^{-\frac{Q}{RT}} \tag{4}$$

where K is a constant, σ the applied stress, n the stress exponent, Q an activation energy, T the temperature and $R = 8.314$ kJ/mol/K the universal gas constant. K, Q and n depend on the stress level and hence on the creep mechanism considered (diffusion or dislocation creep). A review of current values for these parameters was done by Seltzer [Seltzer et al., 1971] and more recently by Monerie and Gatt [Monerie and Gatt, 2006].

In our experiments, the pronounced hardening requires the definition of an arbitrary stress level if one wants to apply a power law. In the following interpretation of the test data, the value of the stress at a strain of 2% was used to calculate the parameters of the power law. The stress exponent n is deduced for each temperature from Figure 10 where the stresses at 2% strain are plotted in function of the strain rate (log-log scale). The linear regressions did not all lead to the same value of n regardless of the temperature but to exponents between 16 and 25. Similar values have already been obtained in tests performed at moderate to high strain rates, i.e., 10^{-3}-10^{-2}/s [Guérin, 1975,Tachibana et al., 1976]. They are far from the 3 to 7 exponents identified from creep or bending tests. These high values show that the material tends to be less viscous as the strain rate increases.

To estimate the activation energy Q, we plot $\ln \dot{\varepsilon}/\sigma^n$ versus $1/RT$ as shown in Figure 11. A stress exponent n of 18 is used. The slope of the

linear regression gives an activation energy of 549 kJ/mol. Values of the same order were already obtained ([Guérin, 1975] 462 kJ/mol, [Dherbey et al., 2002] 524 kJ/mol, [Bohaboy et al., 1969] 552 kJ/mol) from creep or strain-rate driven tests. They are usually attributed to a dislocation creep mechanism [Seltzer et al., 1971] which is consistent with the high stress (> 60 MPa) and temperature level in our tests. They are close to the activation energy of uranium self-diffusion (Q = 577 kJ/mol).

These results confirm that a single power law is not adequate to model the strains of uranium dioxide over the whole range of strain rates it can encounter during a RIA. As suggested by several authors, the stress exponent $n \sim 16 - 25$ obtained at high strain rates and high stresses might be the signature of a Peierls mechanism with no specific microstructural features [Nadeau, 1969, Tachibana et al., 1976, Canon et al., 1971].

In the next Section, we will introduce a constitutive model able to describe UO_2 behaviour in the moderate to high strain rate range.

3 Modelling and simulation

3.1 Constitutive model

In 2002, Dherbey et al. [Dherbey et al., 2002] proposed an alternative model for uranium dioxide creep, based on a unique hyperbolic sine law. The original idea came from the fact that diffusion creep was not present in coarse grain samples (grain size 36 μm). The usual separation in two creep mechanisms appeared therefore more apparent than real. With the hyperbolic sine law, they were able to reproduce their data over the whole range of stresses (10-80 MPa) and temperatures (1365 - 1575°C) considered. Recently, Soulacroix et al. [Soulacroix et al., 2013] successfully used a similar function to fit the test data of Guérin [Guérin, 1975] and particularly the strain rate dependency.

In 2006, Monerie and Gatt [Monerie and Gatt, 2006] introduced material volume variation in the standard two power laws model. The hollow sphere model of Michel and Suquet [Michel and Suquet, 1992] was considered to account for pore compressibility. The formulation of the model is based on the definition of a quadratic macroscopic potential Ψ dependent on the first and second invariants of the stress tensor.

In our experiments, a non constant stress exponent n and densification (negative pore volume evolution) were simultaneously observed. We therefore propose here to use a hyperbolic sine law to cover a large stress-strain rate domain and add pore compressibility. To this end, the following macroscopic

potential is defined:

$$\Psi(\sigma_m, \sigma_{eq}, f) = \sigma_0 K e^{-\frac{Q}{RT}} \cosh\left(\frac{\Sigma}{\sigma_0}\right) \tag{5}$$

where $\Sigma = \sqrt{\alpha {\sigma_m}^2 + \beta {\sigma_{eq}}^2}$ is an equivalent stress which depends on the hydrostatic stress $\sigma_m = \frac{1}{3}\ \boldsymbol{\sigma} : \mathbf{1}$ and on the second invariant of the stress tensor $\sigma_{eq} = \sqrt{\frac{3}{2}\boldsymbol{s} : \boldsymbol{s}}$ (with $\boldsymbol{\sigma}$ the stress tensor, $\mathbf{1}$ the unit tensor and $\boldsymbol{s} = \boldsymbol{\sigma} - \sigma_m \mathbf{1}$ the deviatoric stress tensor). f is the porosity volume fraction. The two parameters $\alpha(f)$ and $\beta(f)$ define the relative contribution of the hydrostatic σ_m and of the deviatoric stresses σ_{eq} to the strain rate. σ_0 and K are constant parameters. Q is the activation energy. The macroscopic viscoplastic strain rate tensor $\dot{\boldsymbol{\varepsilon}}^{vp}$ is given as follows by the derivation of equation 5 with respect to stress:

$$\dot{\boldsymbol{\varepsilon}}^{vp} = \frac{\partial \Psi}{\partial \boldsymbol{\sigma}} = K e^{-\frac{Q}{RT}} \sinh\left(\frac{\Sigma}{\sigma_0}\right) \left(\frac{1}{3}\alpha \frac{\sigma_m}{\Sigma}\mathbf{1} + \frac{3}{2}\beta \frac{\boldsymbol{s}}{\Sigma}\right) \tag{6}$$

As proposed by Monerie and Gatt [Monerie and Gatt, 2006], the following mass balance is used to describe porosity volume fraction evolution:

$$\dot{f} = (1-f)\dot{\boldsymbol{\varepsilon}}^{vp} : \mathbf{1} = (1-f) K e^{-\frac{Q}{RT}} \sinh\left(\frac{\Sigma}{\sigma_0}\right) \alpha \frac{\sigma_m}{\Sigma} \tag{7}$$

3.2 Parameters identification

The model is completely defined if the five parameters K, Q, σ_0, α and β are known. A rough estimation can be obtained assuming that the compression tests led to a homogeneous stress state in the samples and that most of the prescribed strain is viscoplastic (neglecting elastic strains). In this case, the stress tensor has one component $\sigma_{zz} = -\sigma$ with $\sigma > 0$ the magnitude of the axial stress ($\sigma_m = -\frac{1}{3}\sigma$ and $\sigma_{eq} = \sigma$). By simple mathematics, one can show that the axial strain rate $\dot{\varepsilon}_{zz}$ is related as follows to the stress σ:

$$\dot{\varepsilon}_{zz} \approx \dot{\varepsilon}^{vp}_{zz} = -K \frac{\alpha + \beta}{\sqrt{\frac{1}{9}\alpha + \beta}} e^{-\frac{Q}{RT}} \sinh\left(\frac{\sigma\sqrt{\frac{1}{9}\alpha + \beta}}{\sigma_0}\right) \tag{8}$$

In a first approximation, the pore compressibility can also be neglected ($\alpha = 0$ and $\beta = 1$) leading to the following simple expression:

$$\dot{\varepsilon}_{zz} = -K e^{-\frac{Q}{RT}} \sinh\left(\frac{\sigma}{\sigma_0}\right) \tag{9}$$

From the tests results presented in Section 2 (stress at 2% strain, temperature, strain rate), the three parameters K, σ_0 and Q of Equation 9 can be readily obtained using a standard Excel spreadsheet with a numerical solver. The initialization of the parameters is based on an exponential fit of the strain rate - stress datapoints ($\sigma_0 \approx 6$ MPa) and on the activation energy obtained previously from the power law fit (≈ 500 kJ/mol). In Figure 12, the calculated versus experimental stresses are plotted. The dotted lines indicate the ± 10 MPa interval. With $K = 29130$/s, $\sigma_0 = 5$ MPa and $Q = 482$ kJ/mol, most of the calculated stresses fall in the ± 10 MPa interval (Figure 12 top). Only the 1100°C data points are out of the domain. This particular behaviour at low temperatures and high stresses has been ascribed by Dherbey and al. [Dherbey et al., 2002] to an additional sort of barrier to the movement of dislocations, i.e., a Peierls force or lattice resistance [Ashby, 1972]. It can be accounted for in the model by a slight modification of the activation energy Q with temperature:

$$Q = \max(482; 876 - 0.0025T) \text{ kJ/mol} \tag{10}$$

Figure 12 (bottom) shows the satisfactory agreement between calculated and experimental stresses obtained with this expression for the activation energy. At 1100°C, $Q = 546$ kJ/mol. This value remains consistent with a dislocation based creep mechanism (Q = 480 - 580 kJ/mol as discussed in section 2.4). The extrapolation of Equations 9 and 10 to smaller temperatures leads to increasing stresses with decreasing temperatures, as obtained in the experiments of Guérin [Guérin, 1975] (600, 800, 900 and 1100°C). At 25°C, a maximum stress ~ 1000 MPa is calculated, consistent with the compression strength of non heated uranium dioxide measured by Igata and Domoto [Igata and Domoto, 1973].

The two remaining coefficients α and β can be estimated by analogy with the compressibility included in the power law model of Monerie and Gatt [Monerie and Gatt, 2006]. Assuming again that the compression test led to a uniform stress state in the samples but this time without neglecting pore compressibility, equation 7 reduces to:

$$\dot{f} = -(1-f)K\frac{\alpha}{\sqrt{\frac{1}{9}\alpha+\beta}}e^{-\frac{Q}{RT}}\sinh\left(\frac{\sigma\sqrt{\frac{1}{9}\alpha+\beta}}{\sigma_0}\right) \tag{11}$$

Comparing this expression to equation 8 for the strain rate leads to:

$$\dot{f} = (1-f)\frac{\alpha}{\alpha+\beta}\dot{\varepsilon}_{zz} \tag{12}$$

The rate of porosity evolution in a compression test depends directly on the applied strain rate (neglecting elastic strains).

The formulation proposed by Monerie and Gatt [Monerie and Gatt, 2006] is based on a micro-macro approach. Uranium dioxide is considered as an incompressible isotropic matrix with randomly distributed pores. The compressibility of the pores explains the volume variation of the material at the macroscopic scale. The behaviour of the incompressible matrix is described by power laws similar to equation 4. The hollow sphere model of Michel and Suquet [Michel and Suquet, 1992] is used to define the parameters of the macroscopic potential from which the viscoplastic strain rate tensor is derived. The equivalent stress Σ in their model takes the following form:

$$\Sigma = \sqrt{\frac{9}{4} A {\sigma_m}^2 + B {\sigma_{eq}}^2} \tag{13}$$

where A and B are given in function of the porosity f and of the stress exponent n of the power law by:

$$A(f) = \left(n \left(f^{-\frac{1}{n}} - 1 \right) \right)^{-\frac{2n}{n+1}} \tag{14}$$

$$B(f) = \left(1 + \frac{2}{3} f \right) (1-f)^{-\frac{2n}{n+1}} \tag{15}$$

The parameters $A(f)$ and $B(f)$ ensure that the incompressible viscoplastic behaviour of the matrix is recovered when the porosity tends to zero ($A(f) \to 0$ when $f \to 0$ and $B(f) \to 1$ when $f \to 0$). The formalism proposed by Monerie and Gatt [Monerie and Gatt, 2006] leads, in case of a uniaxial compression test, to the following expression for the porosity evolution rate:

$$\dot{f} = (1-f) \frac{A}{A + \frac{4}{9} B} \dot{\varepsilon}_{zz} \tag{16}$$

The comparison of equations 12 and 16 shows that the compressible hyperbolic sine and power law models will give a similar porosity evolution rate (in uniaxial compression) if :

$$\frac{\alpha}{\beta} = \frac{9}{4} \frac{A}{B} \tag{17}$$

Thus, any combination of (α,β) parameters that satisfies condition 17 is suitable. In the simulations that follow, we chose $\alpha = \frac{9}{4} A(f)$ and $\beta = B(f)$ with a stress exponent $n = 6$. A value of 6.2 was used by Dherbey [Dherbey et al., 2002] to fit their test data at high stress level.

3.3 Numerical implementation

The hyperbolic sine model was readily implemented using a code generator called MFront which is developed by the CEA. MFront allows the user to write constitutive equations in a way which is very similar to their mathematical expressions, notably by providing an appropriate tensorial formalism [Helfer et al., 2009]. MFront turns the user's behaviour implementation into optimised C++ sources which can be plugged into several mechanical solvers. The simulations reported in this paper were performed using Cast3M, the CEA finite element solver [Cast3m, 2010].

The constitutive equations are written using the standard small-strain formalism based on an additive partitioning of the total strain into an elastic and a viscoplastic part:

$$\boldsymbol{\sigma} = \boldsymbol{C} : \boldsymbol{\varepsilon}^e = \boldsymbol{C} : (\boldsymbol{\varepsilon} - \boldsymbol{\varepsilon}^{vp}) \tag{18}$$

where $\boldsymbol{C}$ is the fourth order elastic tensor and $\boldsymbol{\varepsilon}^e$ the elastic strain tensor. An implicit numerical scheme is used to solve the system with the main unknowns as the six components of the elastic strain tensor, the equivalent viscoplastic strain defined by $\boldsymbol{\varepsilon}^{vp} : \boldsymbol{\varepsilon}^{vp}$ and the porosity f.

The system of equations 6, 7 and 18 has been solved in finite strain computations using two distinct approaches:

- a hypoelastic eulerian formulation provided by the Cast3M finite element solver. Cast3M implementation is close to the one described by Simo and Hugues [Simo and Hughes, 1998] ;

- the lagrangian logarithmic strains proposed by Miehe and al. [Miehe et al., 2002] and provided by MFront. This approach is consistent with the definition of the strains given earlier in this paper.

For the creep tests with monotonic loading considered here, these two approaches were found to give similar results, a fact also reported by Doghri [Doghri, 2000] in another context.

3.4 Simulation of strain rate driven tests

As discussed in Section 2, the stress state in the samples tested in compression is far from being uniaxial. Friction at the upper and lower ends tends to generate a three-dimensional stress state. As a consequence, densification was observed preferentially at the samples' core. The important axial and hoop strains reached during the tests suggest that structural non linearities (large deformations) might be of importance when analysing the results.

The mesh and boundary conditions used in the simulations are presented in Figure 13. Only half of the pellet is meshed with quadratic elements assuming two-dimensional axisymmetry. The upper and lower tungsten plates are not directly taken into account. The strong friction at pellet ends is described by the boundary conditions: the radial displacement of the upper and lower surface is forbidden. Structural behaviour is taken into account by using the large displacements scheme of Cast3M [Cast3m, 2010]. A constant axial displacement rate between 0.01 and 100 mm/s (depending on the test simulated) is then prescribed on the upper surface of the pellet. The maximum prescribed axial displacement matches the experimental value to ease the comparison of residual strains. The thermal strains are taken into account prior to the displacement-driven phase. They are substracted at the end of the simulation.

The modulus of elasticity E and Poisson ratio ν considered in the simulations are based on Martin et al. [Martin, 1989]. They are expressed in function of the temperature T (in K) and of the porosity f as follows:

$$E = (1 - 2.5f)(226.93 - 1.5399 \times 10^{-2}T - 9.597 \times 10^{-6}T^2) \tag{19}$$

E is given in GPa. ν is constant and equal to 0.3. The initial porosity of uranium dioxide considered in the simulations was based on the average relative density measured prior to testing: $f_0 = 0.036$.

Figure 14 shows the experimental and simulated stress-strain curves for all the tests. The model reproduces correctly the strain rate and temperature dependency. The apparent strain hardening during the tests is partly recovered in the simulations. The calculated slope of the stress-strain curves tends to increase with the strain rate and decrease with temperature. These results are consistent with the experimental curves. The magnitude of strain hardening is however not well caught at high stresses (high strain rates and low temperatures). Material plastic hardening rather than structural hardening could be at the origin of these differences.

Figure 15 gives the calculated and measured axial diameter profiles of the pellets at the end of all the tests. The barrel shape of the pellet is well reproduced in the simulation owing to the boundary conditions on the top and bottom surfaces. The magnitude of diameter increase during the tests is also well captured in the simulations.

Figure 16 illustrates the calculated distribution of axial-hoop strains, of axial-hoop stresses, of the second stress invariant and of the porosity during the test at 1700°C and 10^{-3}/s. As expected from the barrel shape, there is a pronounced axial gradient in the axial and hoop strains distribution ($\varepsilon_{zz}(z)$ and $\varepsilon_{\theta\theta}(z)$). While the radial and axial deformations of the upper and lower

parts of the pellet are small, the axial and hoop strains in the central part of the pellet reach -28% and 17%, respectively. These values have to be compared to the average axial and hoop strains at mid-pellet height: -18% and 13% respectively. A radial gradient is also apparent in Figure 16. The axial and hoop strains tend to decrease when approaching the periphery of the pellet.

A radial gradient in axial stress is also apparent at mid-pellet height, see Figure 16. The periphery is less stressed (-50 MPa) than the center (-80 MPa). The distribution of hoop stress is different. The top and bottom parts of the pellet are mostly in compression due to the radial constraint. At mid-height, the pellet periphery is surprisingly in tension (20 MPa). These tensile hoop stresses are due to the non uniform densification. In fact, the densification of the material is stronger at the pellet center than at the pellet periphery. This radial densification gradient is similar to a thermal gradient where the shrinkage of the pellet center is hindered by the pellet periphery. In consequence, hoop tensile stresses appear on the external pellet surface.

The reduction of the porosity is controlled by the equivalent stress Σ, see equation 7, and so by the first and second invariants of the stress tensor. However, the contribution of the second invariant to porosity evolution is more important (β is close to 1 while α is less than 0.01). As seen in Figure 16, the second invariant presents radial and axial gradients with minima at the top and bottom of the pellet and a maximum at the pellet center. The periphery lies in between. The reduction of the porosity is therefore faster at the pellet center. Figure 17 gives the calculated porosities of the samples after testing. At the top of the pellet, the residual porosity is equal to the pre-test porosity (3.6%). At the pellet periphery, the residual porosity is close to 2.9%. At the pellet center, it goes down to 2%. It appears that the reduction in porosity is less important at 1100°C in particular when the tests were stopped at a low strain level (6%). The general trends obtained from the simulations are in good agreement with the evolution of the measured surface porosities of Figure 7.

3.5 Simulation of Creep tests

In the previous Section (3.4), it has been checked that the model was able to reproduce the behaviour of a single uranium dioxide material at strain rates between 10^{-4} and 10^{-1}/s.

To assess the validity of the model at lower strain rates, the creep test database available at the CEA has been simulated. It contains 231 tests performed on uranium dioxide pellets with a grain diameter between 5 and 70 μm and an initial porosity between 1 and 6%. The applied stress in the

creep tests is in the interval 20-80 MPa, the test temperature within 1300-1700°C. The tests resulted in stationary creep strain rates, i.e., constant strain rates, between 10^{-9} and 10^{-4}/s.

The model of Section 3.1 was slightly modified to account for the variation in grain size of the pellet materials. The following function for K was used to describe the increase of stationary creep rates with the grain size:

$$K = K_0 e^{\frac{-\gamma}{d-d_0}} \tag{20}$$

with $K_0 = 77400$/s and $\gamma = 5.277$ μm two constant parameters and $d_0 = 4.6$ μm a reference grain diameter. The mechanism behind the grain size dependency of uranium dioxide creep is still a matter of discussion [Gao et al., 2010]. At high stresses and temperature, the creep strain rate is usually considered independent of grain size [Seltzer et al., 1971] or an increasing function of the grain size (Monerie and Gatt used a d^2 dependency for uranium dioxides with $4.5 \leq d \leq 26$ μm [Monerie and Gatt, 2006]). The extensive database of the CEA, where uranium dioxides with grain size up to 70 μm have been tested, showed that the expected increase of the creep stationary strain rate with grain size was actually limited. In consequence, an exponential increasing function with upper limit K_0 is proposed here to model the grain size dependency of uranium dioxide creep.

The mesh and boundary conditions of Figure 13 were also used in the creep test simulations. The measured stationary creep strain rates were used to define the prescribed axial displacement rates (knowing the initial height of the pellets). The axial stresses reached in the simulations just after the elastic part of the stress-strain curves are compared in Figure 18 to the stresses applied in the creep tests. More than 80% of the calculated stresses lie in the confidence interval of ±10 MPa. The smaller stresses which correspond to small strain rates are well captured by the model showing that both the diffusion and dislocation creep regimes can be correctly assessed with a hyperbolic sine model [Dherbey et al., 2002].

Conclusions

In this paper, a three-dimensional model was proposed to describe the behaviour of uranium dioxide in compression. A dedicated series of compression tests was first realized to obtain data at high strain rates ($10^{-4} - 10^{-1}$/s). The general trends were of an increasing axial stress with the strain rate and of a decreasing axial stress with the temperature (1100-1700°C). The post-test SEM image analyses and density measurements revealed a pronounced densification mostly at the pellet center.

A hyperbolic sine model accounting for porosity evolution was proposed to describe the experimental data over the whole range of strain rates and temperatures considered. The Finite Element simulations of the tests showed a good agreement with the measures in terms of stress-strain curves, post-test axial diameter profiles, porosity evolution at the pellet center, periphery and top. The model was then checked against a database of 231 high temperature creep tests (1300-1700°C) performed on uranium dioxide materials with 4-70 μm grain diameters and 1-6% porosity. The model was able to predict in more than 80% of the cases, and within a margin of ± 10 MPa, the applied stress for a given stationary creep strain rate.

The proposed model covers therefore a wide range of strain rates ($10^{-9} - 10^{-1}$/s), stresses ($20 - 250$ MPa) and temperatures ($1100 - 1700$°C) that makes its use possible in fuel performance codes dedicated to normal, off-normal (power ramps) or accidental conditions.

Acknowledgements

The authors would like to thank Julian Soulacroix and Bruno Michel from the CEA for fruitful discussions on the model.

References

[Ashby, 1972] Ashby, M. F. (1972). A first report on deformation-mechanism maps. *Acta Metallurgica*, 20(7):887–897.

[Bohaboy et al., 1969] Bohaboy, P. E., Asamoto, R. R., and Conti, A. E. (1969). Compressive creep characteristics of stoichiometric uranium dioxide. Technical Report GEAP–10054, General Electric Co., Sunnyvale, Calif. Breeder Reactor Development Operation.

[Canon et al., 1971] Canon, R. F., Roberts, J. T. A., and Beals, R. J. (1971). Deformation of UO2 at high temperatures. *Journal of the American Ceramic Society*, 54(2):105–112.

[Cast3m, 2010] Cast3m (2010). http://www-cast3m.cea.fr.

[Cazalis et al., 2007] Cazalis, B., Desquines, J., Poussard, C., Petit, M., Monerie, Y., Bernaudat, C., Yvon, P., and Averty, X. (2007). The prometra program : Fuel cladding mechanical behavior under high strain rate. *Nuclear technology*, 157(3):215–229.

[Dherbey et al., 2002] Dherbey, F., Louchet, F., Mocellin, A., and Leclercq, S. (2002). Elevated temperature creep of polycrystalline uranium dioxide: from microscopic mechanisms to macroscopic behaviour. *Acta Materialia*, 50(6):1495–1505.

[Doghri, 2000] Doghri, I. (2000). *Mechanics of deformable solids: linear, nonlinear, analytical, and computational aspects*. Springer, Berlin; New York.

[Fuketa et al., 2001] Fuketa, T., Sasajima, H., and Sugiyama, T. (2001). Behavior of high-burnup PWR fuels with low-tin zircaloy-4 cladding under reactivity-initiated-accident conditions. *Nuclear technology*, 133(1):50–62.

[Gao et al., 2010] Gao, J.-C., Wang, L.-F., Wang, Y., and Wu, S.-F. (2010). High-temperature creep properties of uranium dioxide pellet. *Transactions of Nonferrous Metals Society of China*, 20(2):238–242.

[Geelhood, 2010] Geelhood, K. (2010). Modeling high burnup RIA tests with FRAPTRAN. In *TopFuel 2010*, Orlando, Florida, USA.

[Guérin, 1975] Guérin, Y. (1975). Etude par compression à hautes températures de la déformation plastique du bioxyde d'uranium polycristallin. *Journal of Nuclear Materials*, 56(1):61–75.

[Helfer et al., 2009] Helfer, T., Brunon, E., Castelier, E., Ravenet, A., and Chauvin, N. (2009). The fuel performance code Celaeno, conception and simulation of fuel elements for gas-cooled fast reactor. In *GLOBAL 2009*, Paris, France.

[Igata and Domoto, 1973] Igata, N. and Domoto, K. (1973). Fracture stress and elastic modulus of uranium dioxide including excess oxygen. *Journal of Nuclear Materials*, 45(4):317–322.

[Martin, 1989] Martin, D. (1989). The elastic constants of polycrystalline UO2 and (U, Pu) mixed oxides: a review and recommendations. *High Temperatures. High Pressures*, 21(1):13–24.

[Michel and Suquet, 1992] Michel, J. C. and Suquet, P. (1992). The constitutive law of nonlinear viscous and porous materials. *Journal of the Mechanics and Physics of Solids*, 40(4):783–812.

[Miehe et al., 2002] Miehe, C., Apel, N., and Lambrecht, M. (2002). Anisotropic additive plasticity in the logarithmic strain space: modular kinematic formulation and implementation based on incremental minimization principles for standard materials. *Computer Methods in Applied Mechanics and Engineering*, 191(47–48):5383–5425.

[Monerie and Gatt, 2006] Monerie, Y. and Gatt, J.-M. (2006). Overall viscoplastic behavior of non-irradiated porous nuclear ceramics. *Mechanics of Materials*, 38(7):608–619.

[Nadeau, 1969] Nadeau, J. S. (1969). Dependence of flow stress on nonstoichiometry in oxygen-rich uranium dioxide at high temperatures. *Journal of the American Ceramic Society*, 52(1):1–7.

[Papin et al., 2007] Papin, J., Cazalis, B., Frizonnet, J. M., Desquines, J., Lemoine, F., Georgenthum, V., Lamare, F., and Petit, M. (2007). Summary and interpretation of the CABRI REP-Na program. *Nuclear Technology*, 157(3):230–250.

[Radford and Terwilliger, 1975] Radford, K. C. and Terwilliger, G. R. (1975). Compressive deformation of polycrystalline UO2. *Journal of the American Ceramic Society*, 58(7-8):274–278.

[Roberts, 1974] Roberts, J. T. A. (1974). Mechanical equation of state and high-temperature deformation (>=0.5Tm) of uranium dioxide. *Acta Metallurgica*, 22(7):873–878.

[Romano et al., 2006] Romano, A., Wallin, H., Zimmermann, M. A., and Chawla, R. (2006). Modelling the CABRI high-burnup RIA test CIP0-1 using an extended version of the FALCON code. *Nuclear Engineering and Design*, 236(3):284–294.

[Sauter and Leclercq, 2003] Sauter, F. and Leclercq, S. (2003). Modeling of the non-monotonous viscoplastic behavior of uranium dioxide. *Journal of Nuclear Materials*, 322(1):1–14.

[Schmitz and Papin, 1999] Schmitz, F. and Papin, J. (1999). High burnup effects on fuel behaviour under accident conditions: the tests CABRI REP-Na. *Journal of Nuclear Materials*, 270(1–2):55–64.

[Seltzer et al., 1971] Seltzer, M. S., Perrin, J. S., Clauer, A. H., and Wilcox, B. A. (1971). Review of creep behavior of ceramic nuclear fuels. *Reactor Technology*, 14(2):99–135.

[Sercombe et al., 2010] Sercombe, J., Fédérici, E., Le Saux, M., Michel, B., and Poussard, C. (2010). 1D and 3D modeling of PCMI during a RIA with ALCYONE V1.1. In *TopFuel 2010*, Orlando, Florida, USA.

[Simo and Hughes, 1998] Simo, J. C. and Hughes, T. J. R. (1998). *Computational inelasticity*. Springer, New York.

[Soulacroix et al., 2013] Soulacroix, J., Michel, B., Gatt, J.-M., Kubler, R., and Barrallier, L. (2013). Comportement micromécanique de l'UO2 : anisotropie du monocristal et contraintes internes associées dans le polycristal. In *21ème Congrès Français de Mécanique*, Bordeaux, France.

[Suzuki et al., 2006] Suzuki, M., Saitou, H., and Fuketa, T. (2006). RANNS code analysis on the local mechanical conditions of cladding of high burnup fuel rods under PCMI in RIA-simulated experiments in NSRR. *Journal of Nuclear Science and Technology*, 43(9):1097–1104.

[Tachibana et al., 1976] Tachibana, T., Furuya, H., and Koizumi, M. (1976). Dependence on strain rate and temperature shown by yield stress of uranium dioxide. *Journal of Nuclear Science and Technology*, 13(9):497–502.

List of Figures

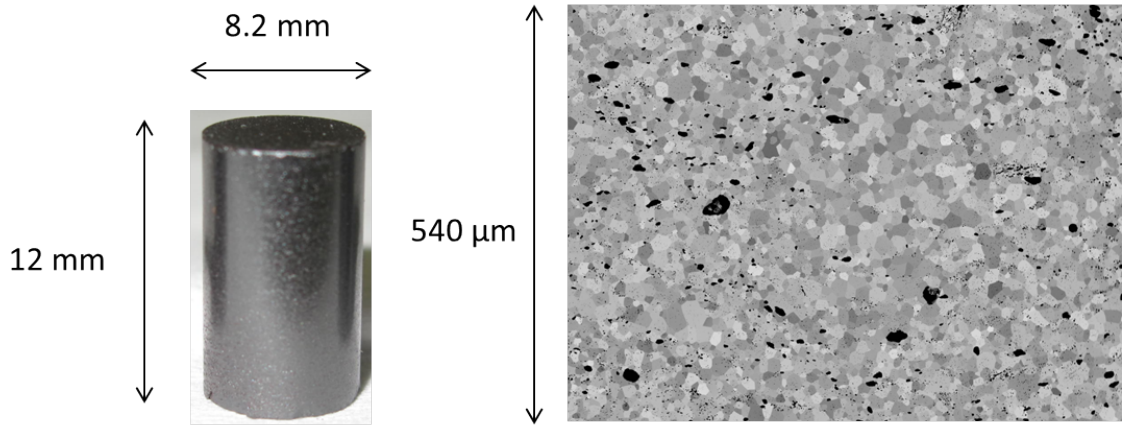

Figure 1: Geometry of the samples and microstructure before testing (SEM).

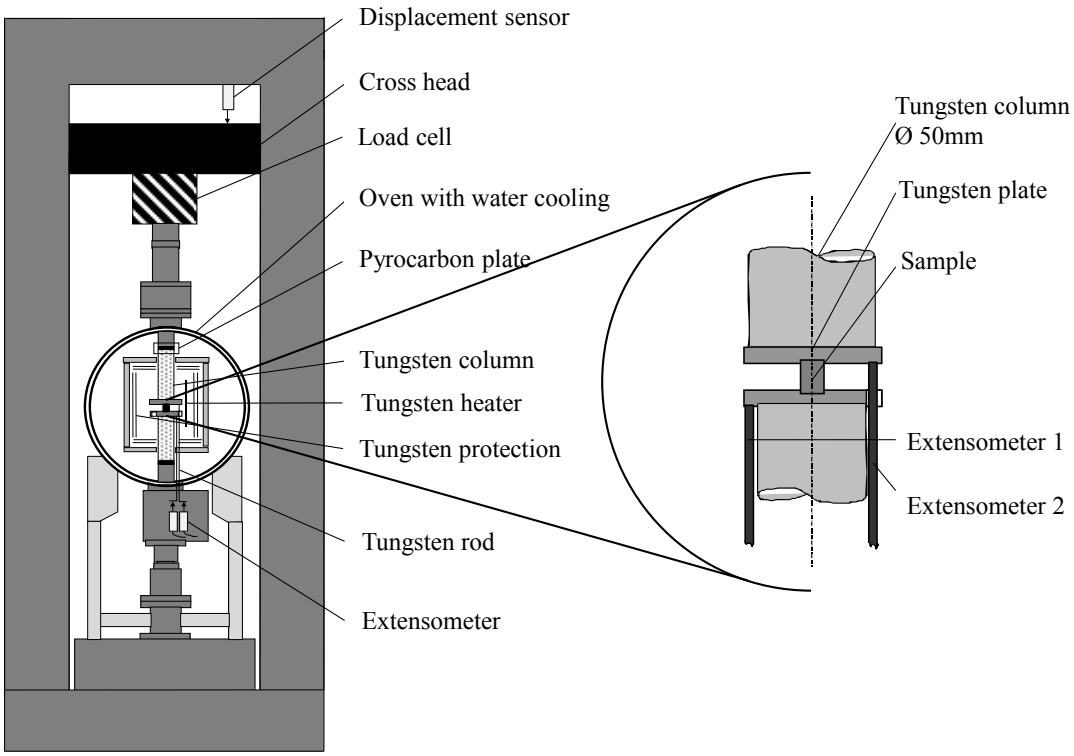

Figure 2: Schematic representation of the testing equipment.

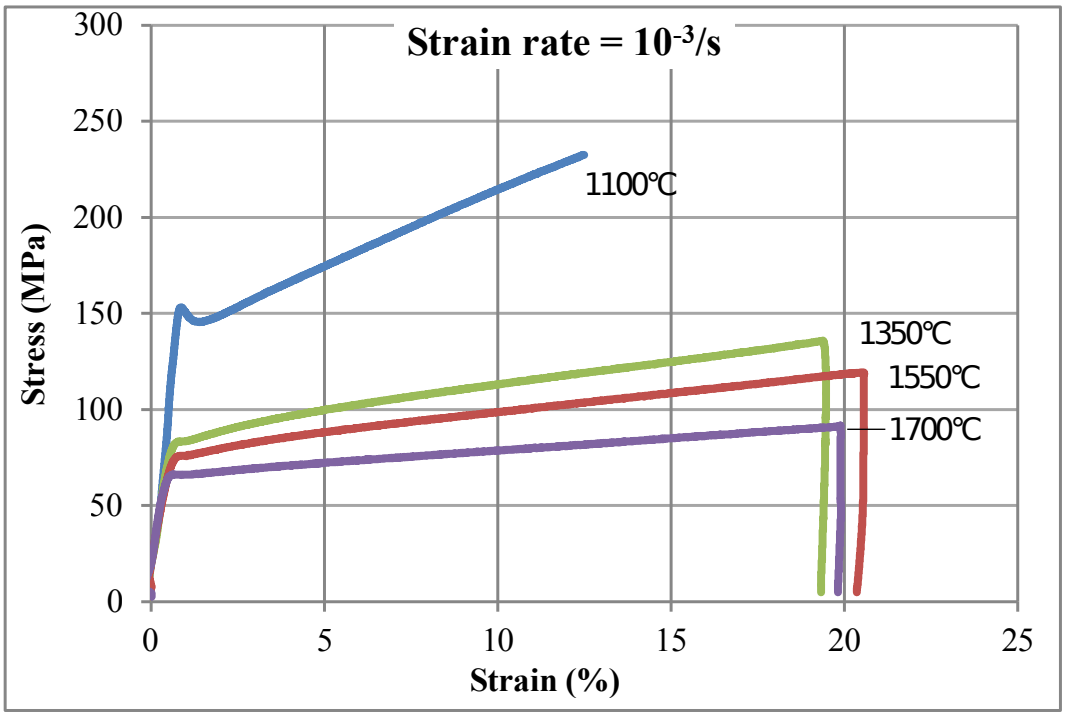

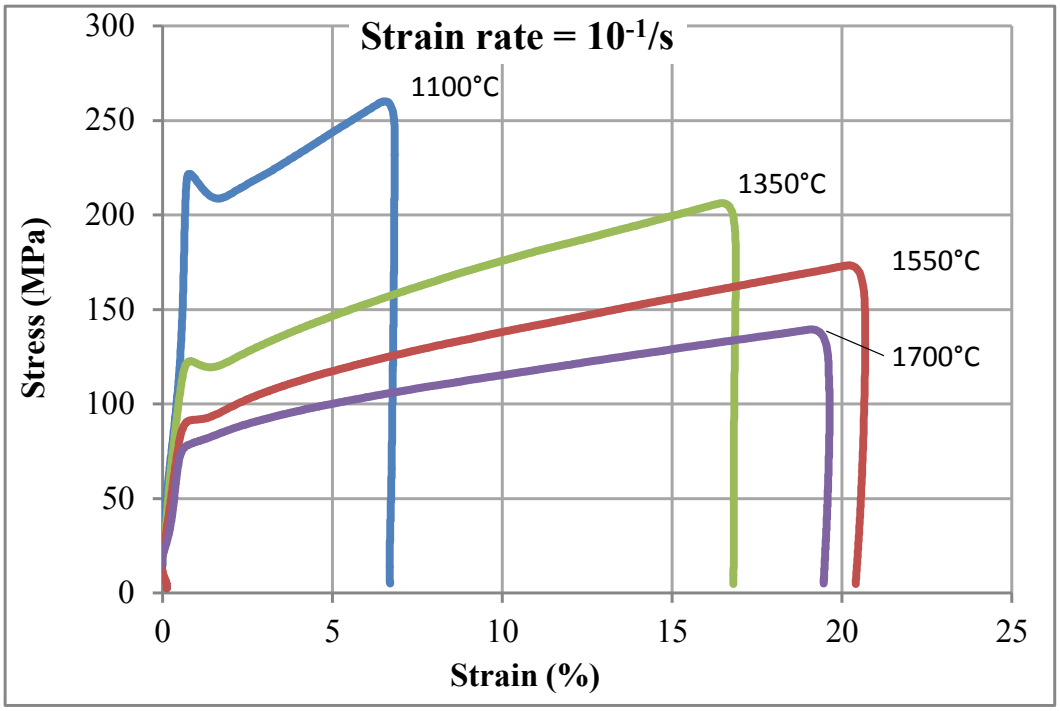

Figure 3: Stress - true strain curves obtained at 10^{-3} and 10^{-1}/s.

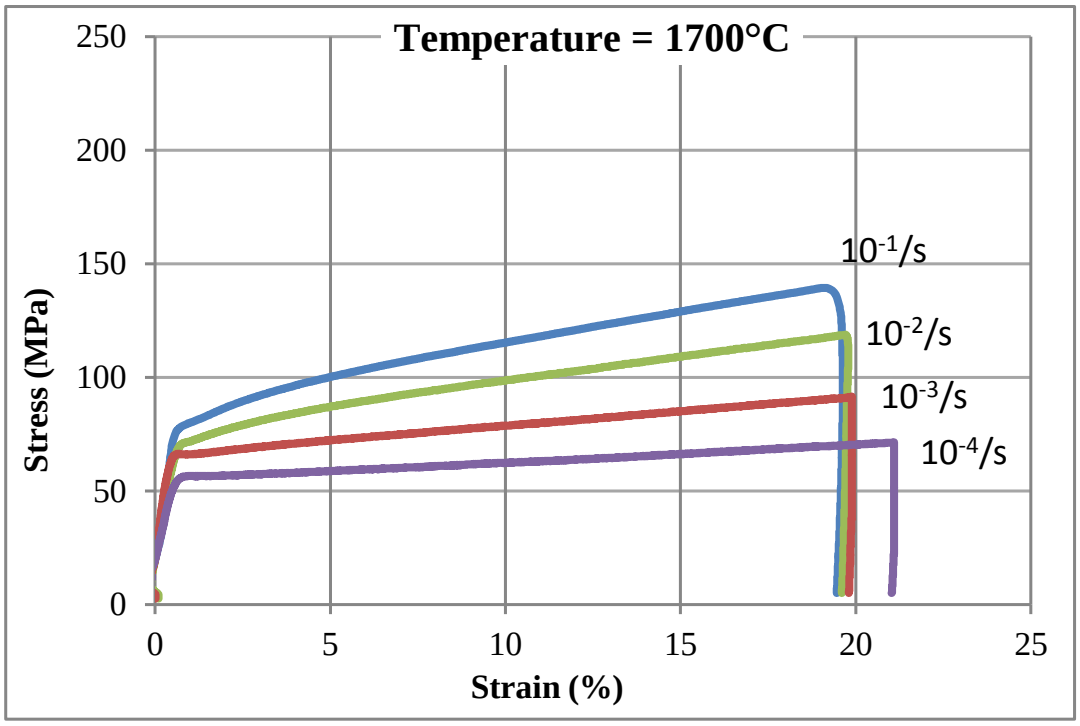

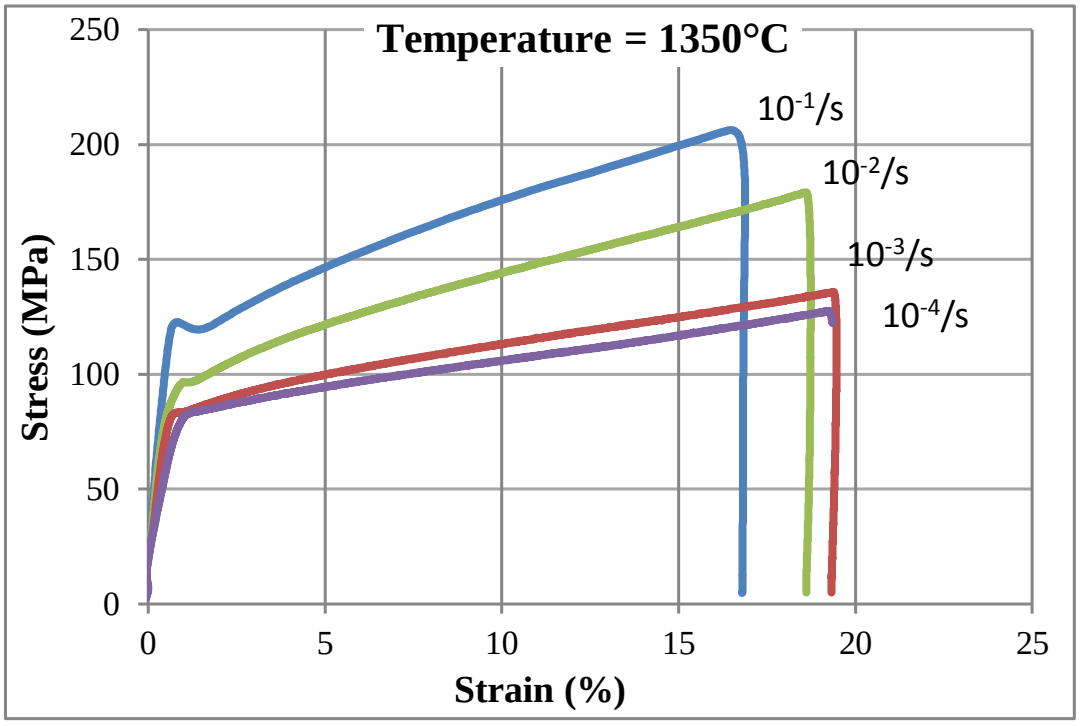

Figure 4: Stress - true strain curves obtained at 1700 and 1350°C.

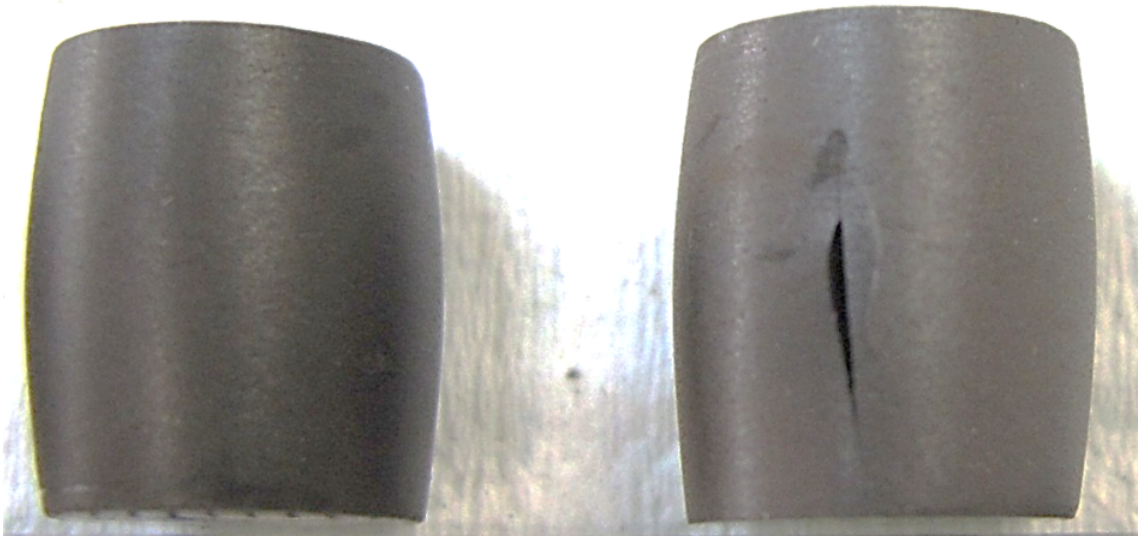

Figure 5: Shape of uncracked and cracked tested samples.

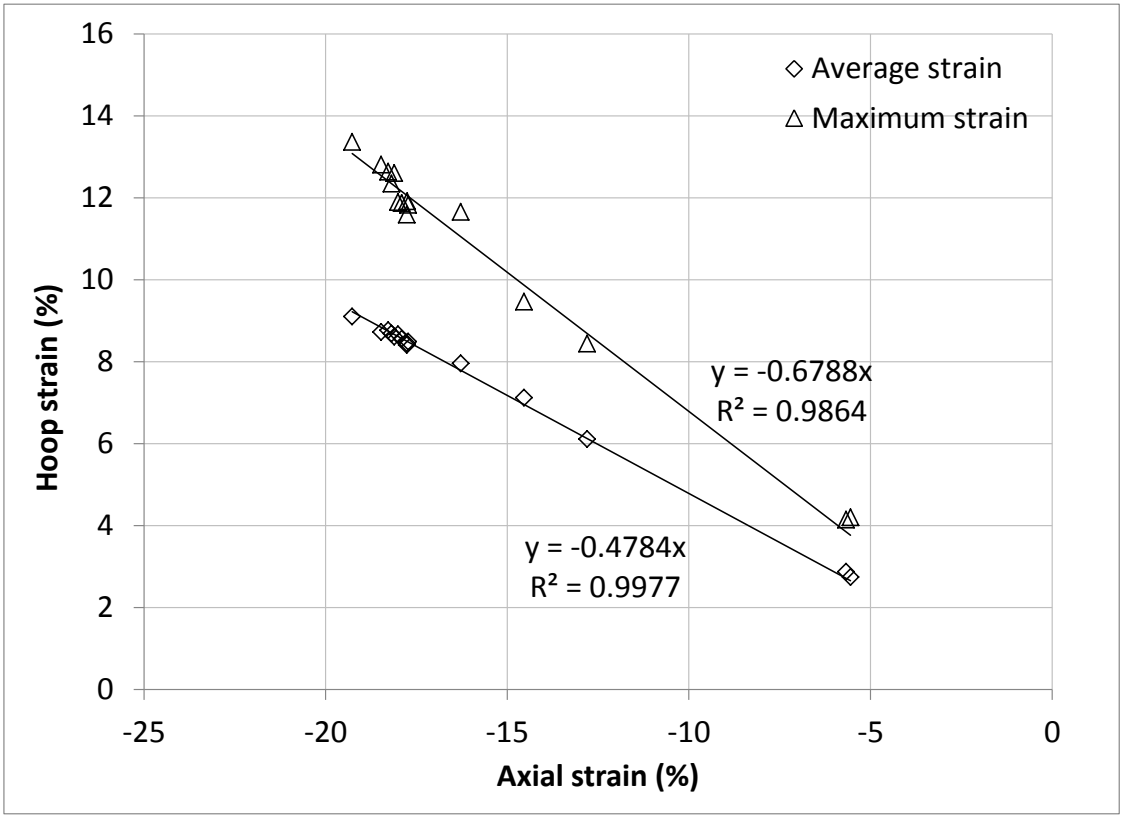

Figure 6: Average and maximum residual hoop strains versus residual axial strains (all tests).

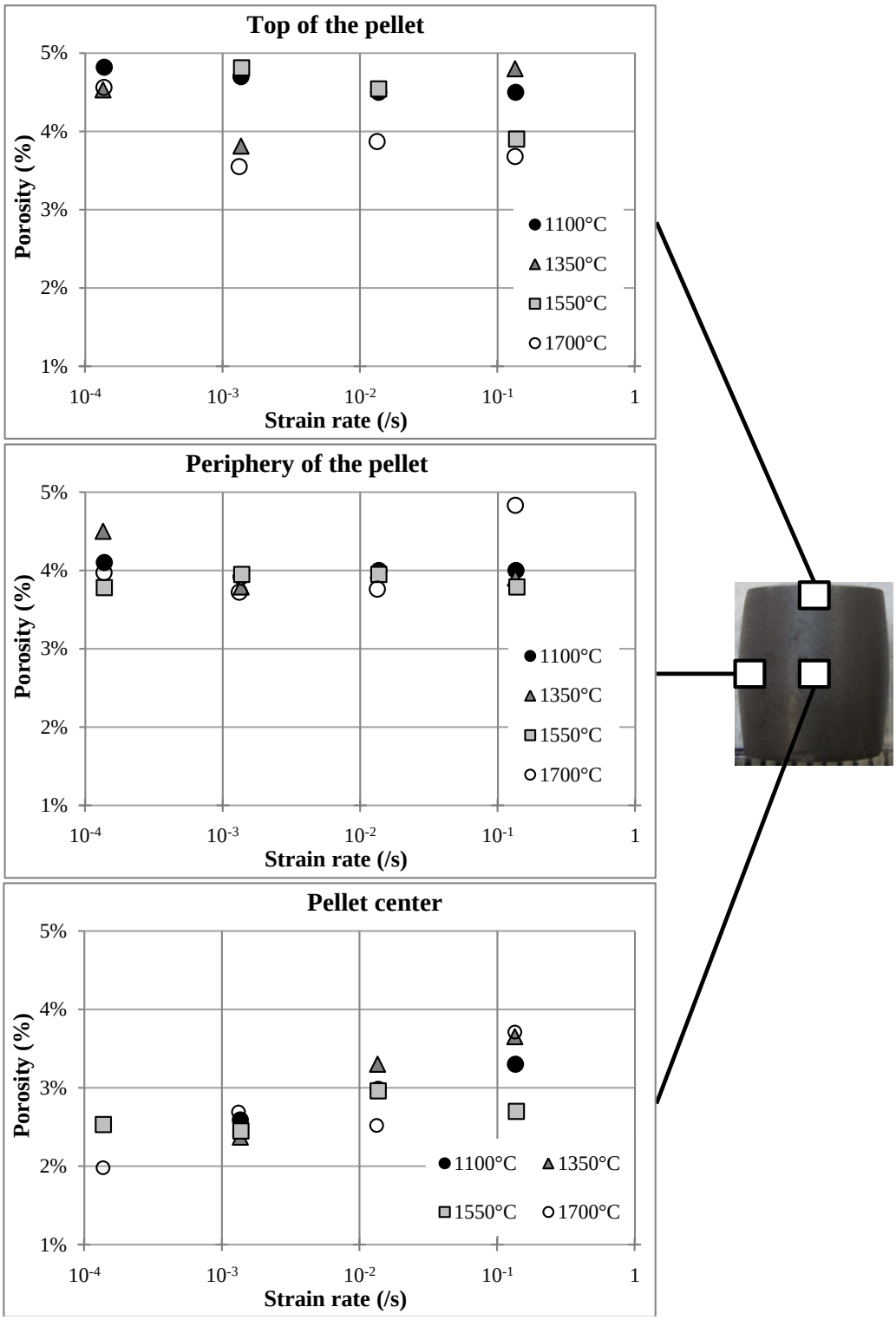

Figure 7: Post-test surface porosities at the top, periphery and center of the samples.

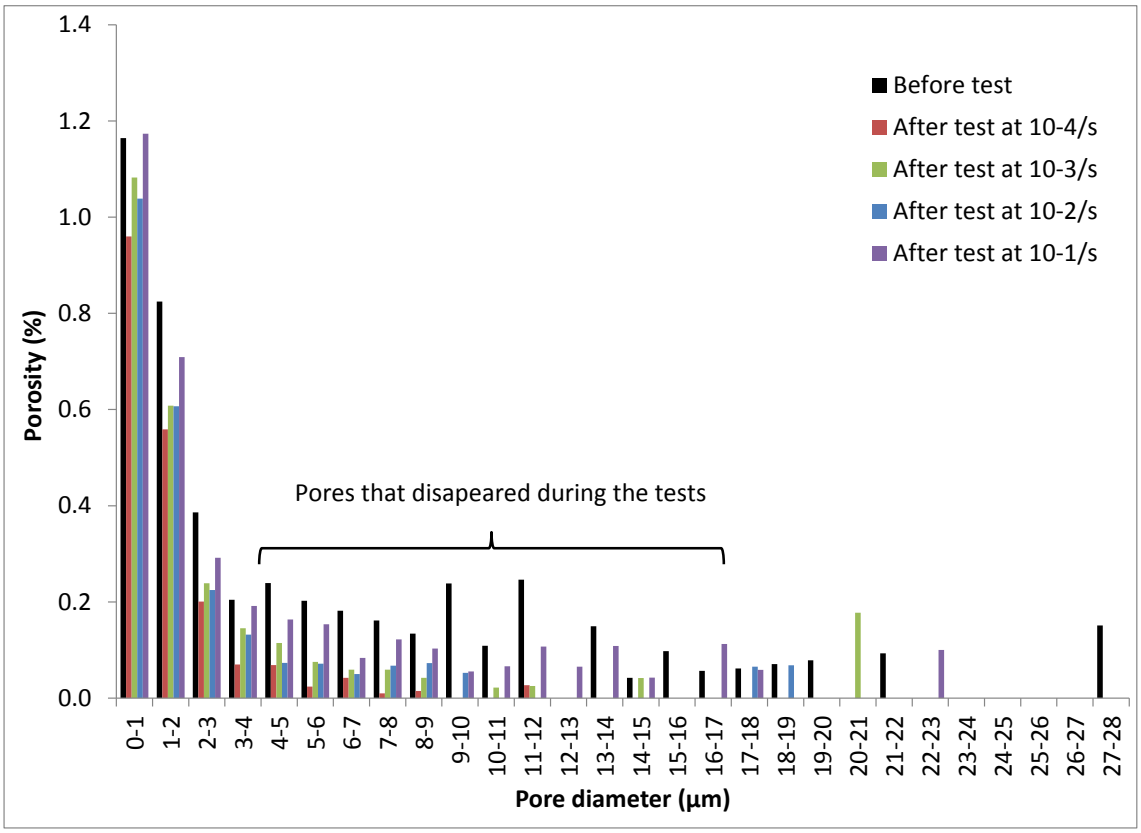

Figure 8: Pore size distribution at the pellet center before and after the tests at 1700°C.

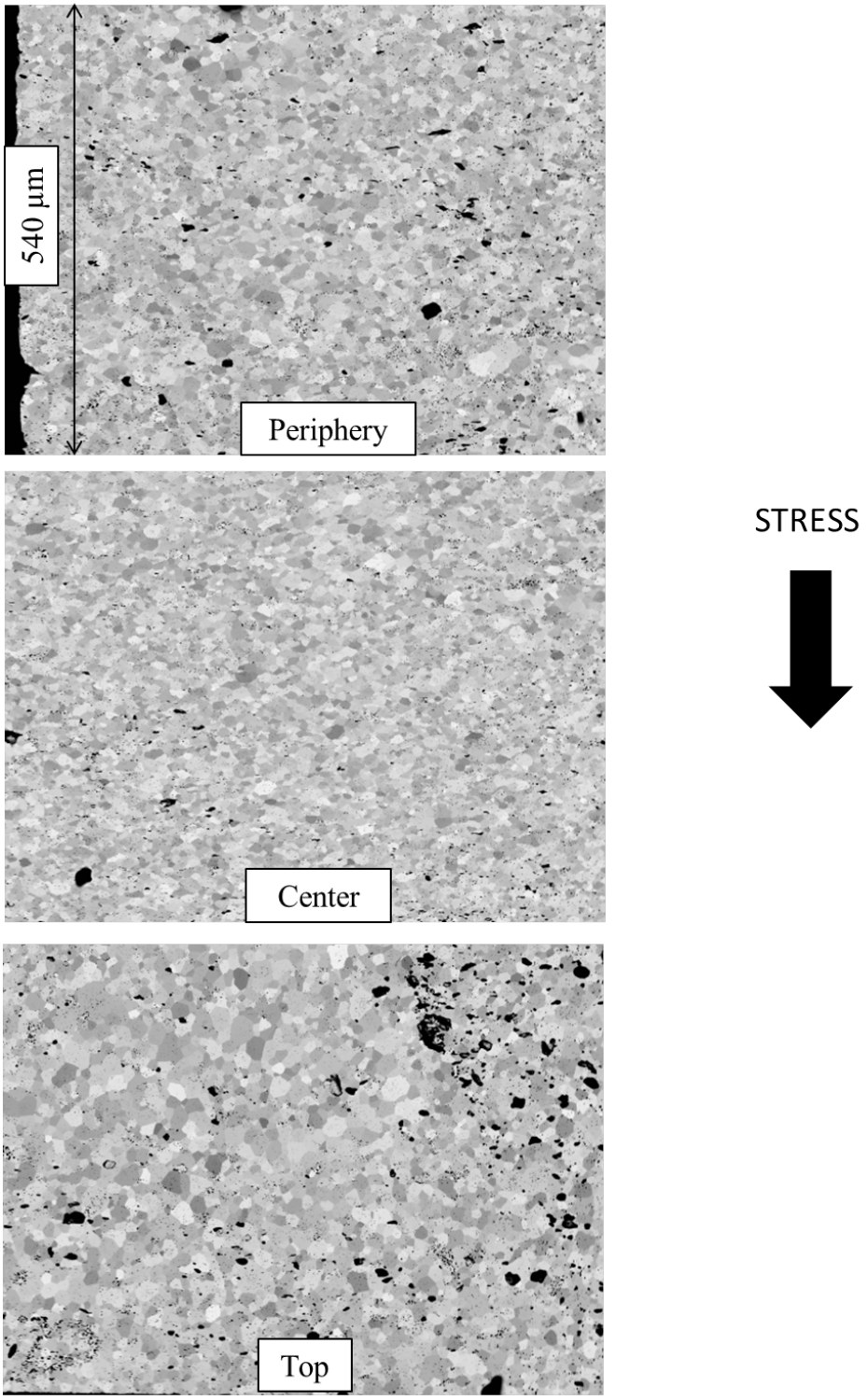

Figure 9: Microstructure of the pellet periphery, center and top after the test at 1550°C and 10^{-4}/s.

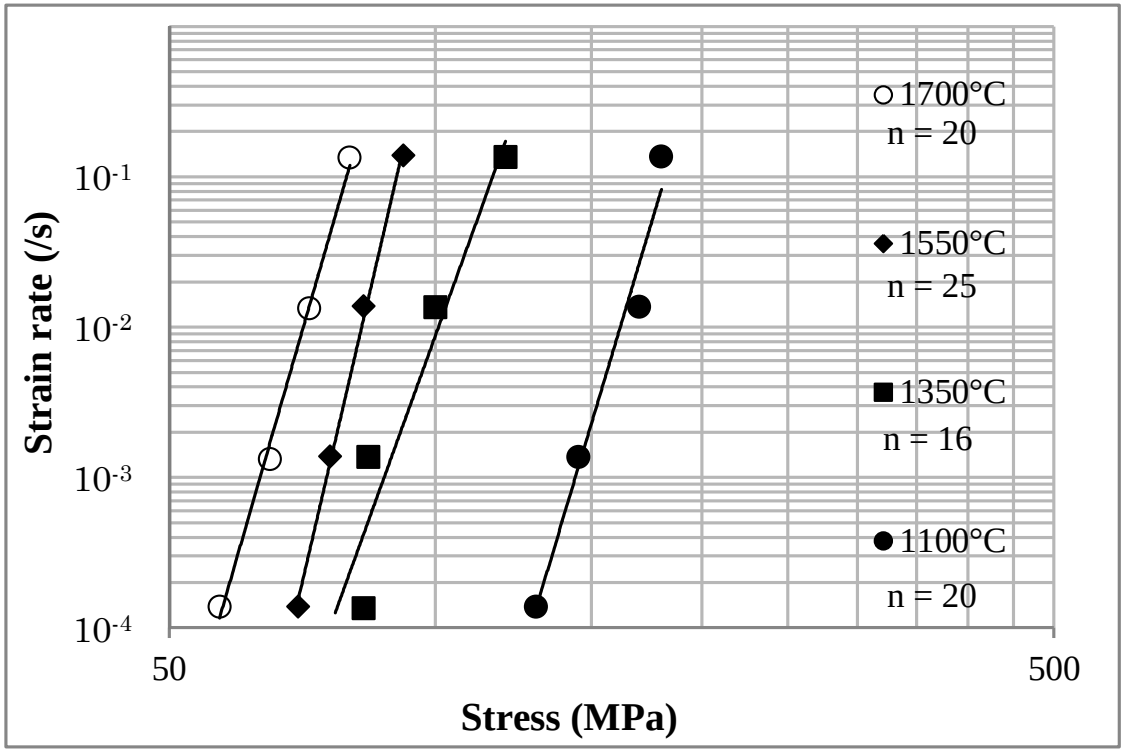

Figure 10: Strain rate versus stress at 2% strain in the tests.

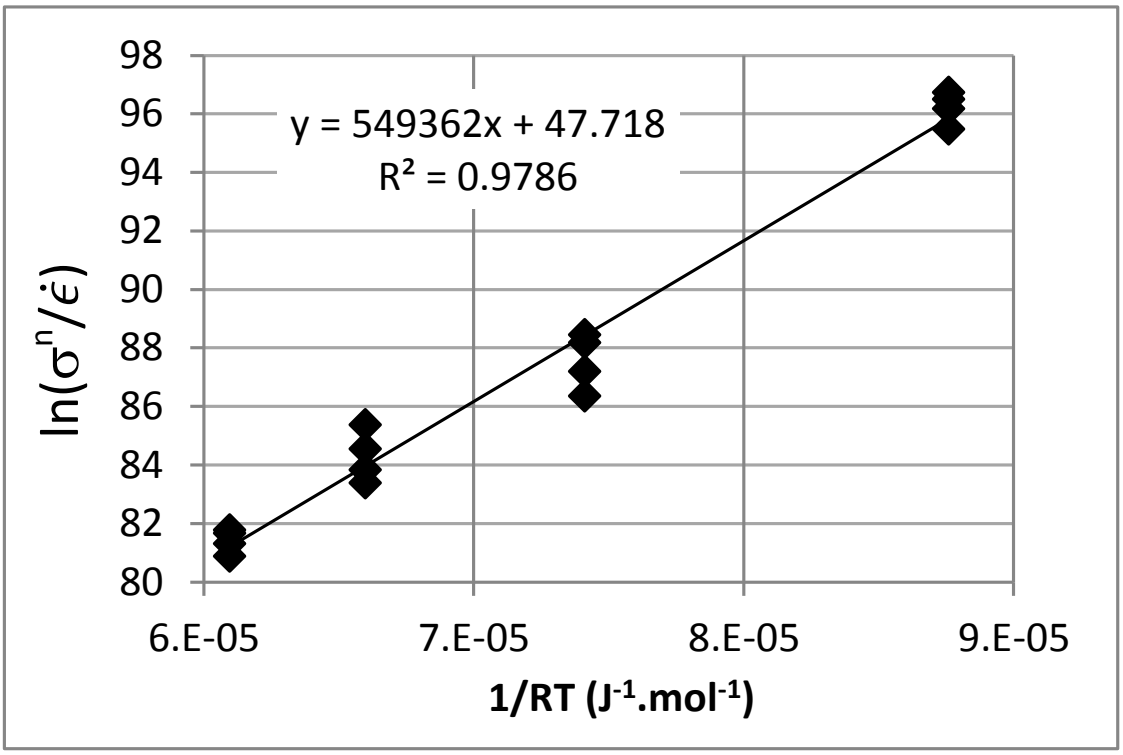

Figure 11: Determination of the activation energy from the test results.

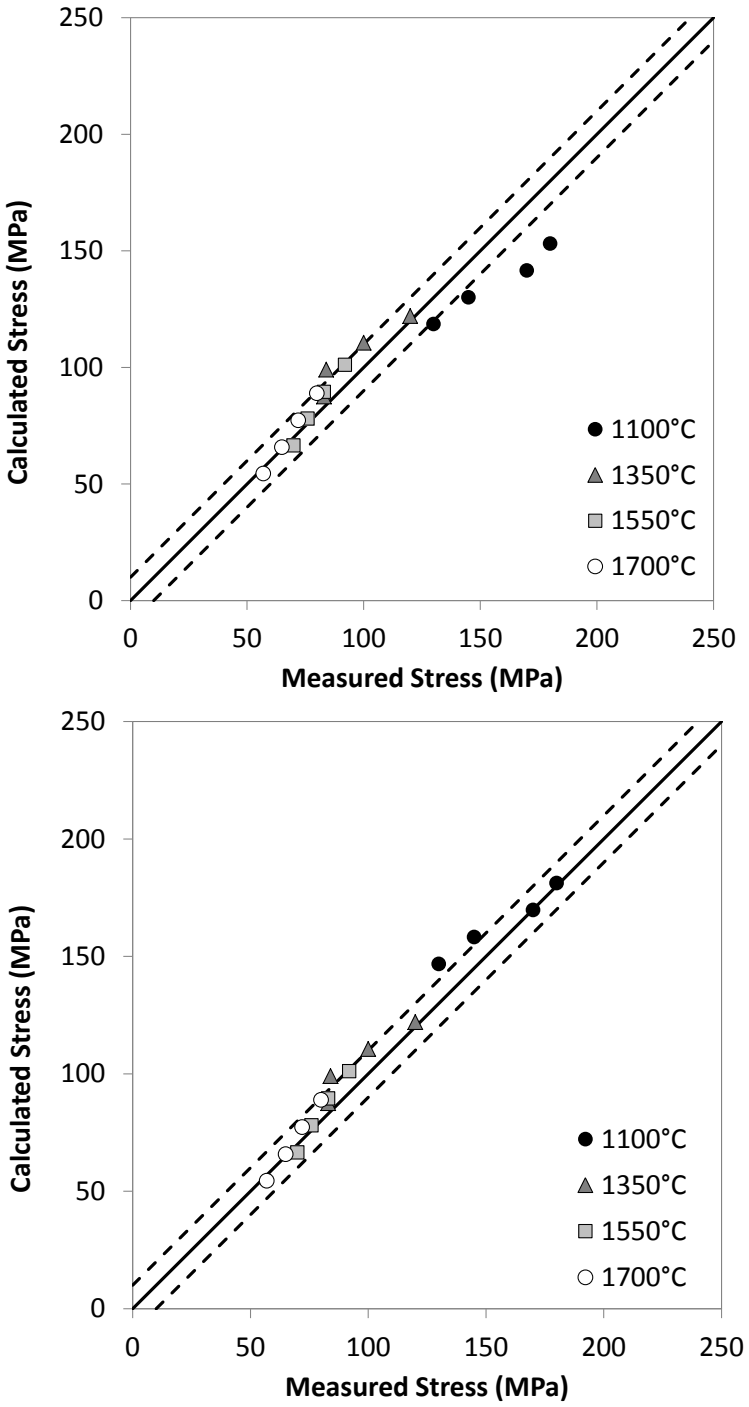

Figure 12: Calculated stresses versus measured stresses in the strain-rate driven tests (top: $K = 29130$/s, $\sigma_0 = 5$ MPa, $Q = 482$ kJ/mol, bottom: $K = 29130$/s, $\sigma_0 = 5$ MPa, $Q = \max(482; 876 - 0.0025T)$ kJ/mol).

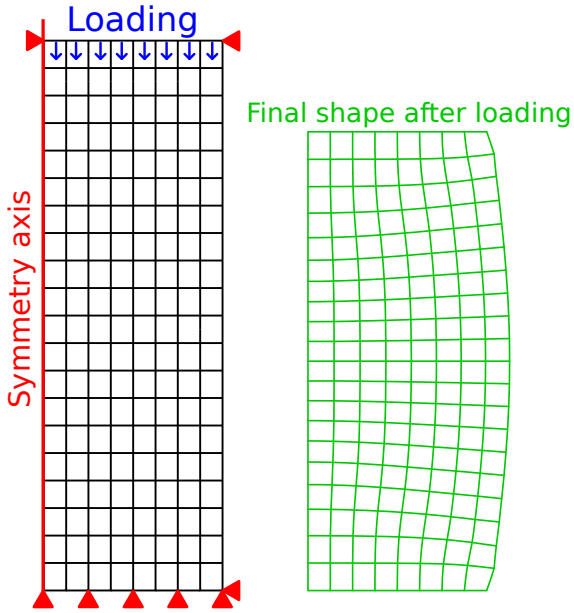

Figure 13: Mesh, boundary conditions and loading (prescribed axial displacement rate) in the simulations of the strain-driven compressive test.

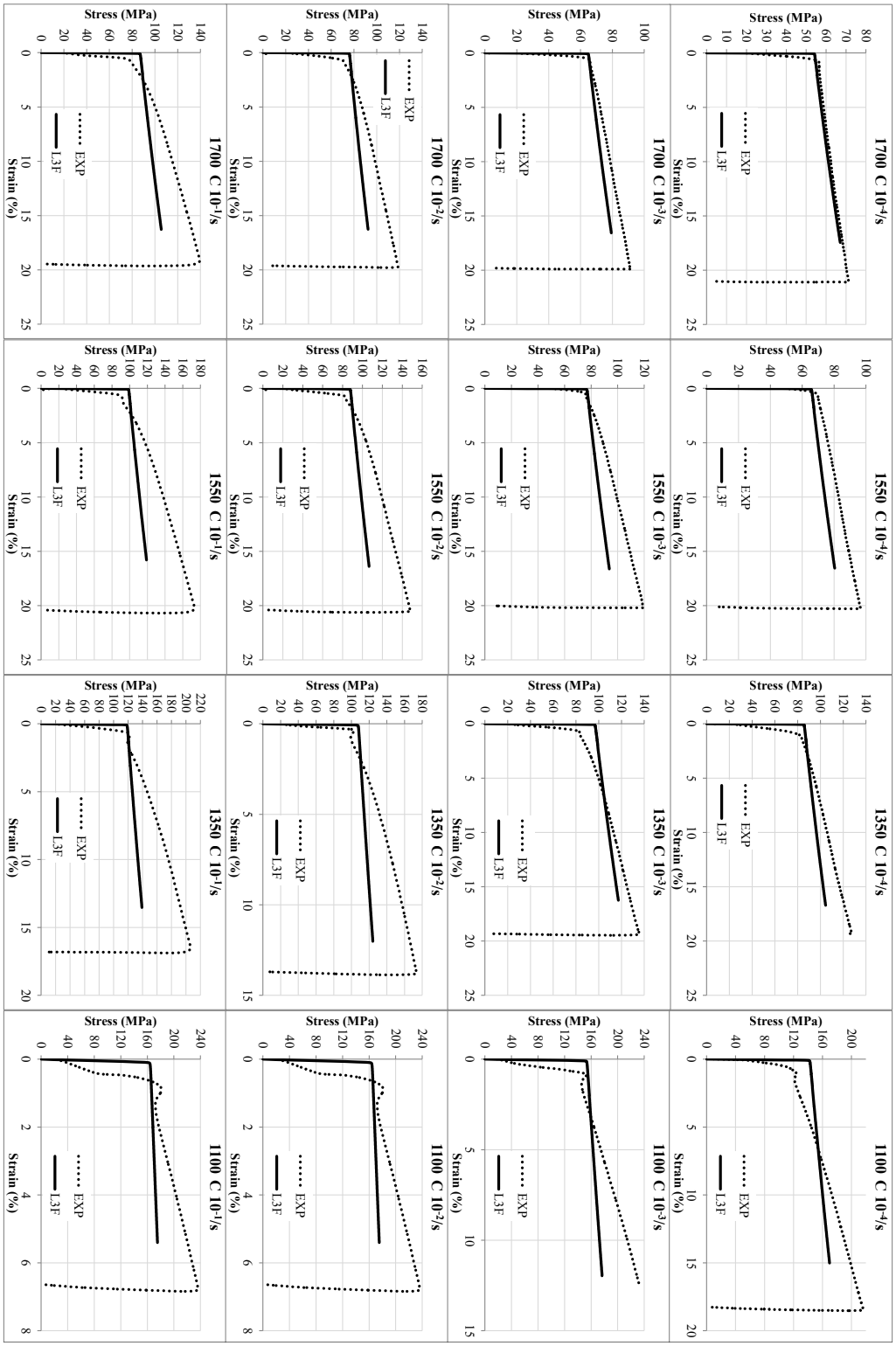

Figure 14: Calculated (L3F) and measured (EXP) stress-strain curves in all the tests.

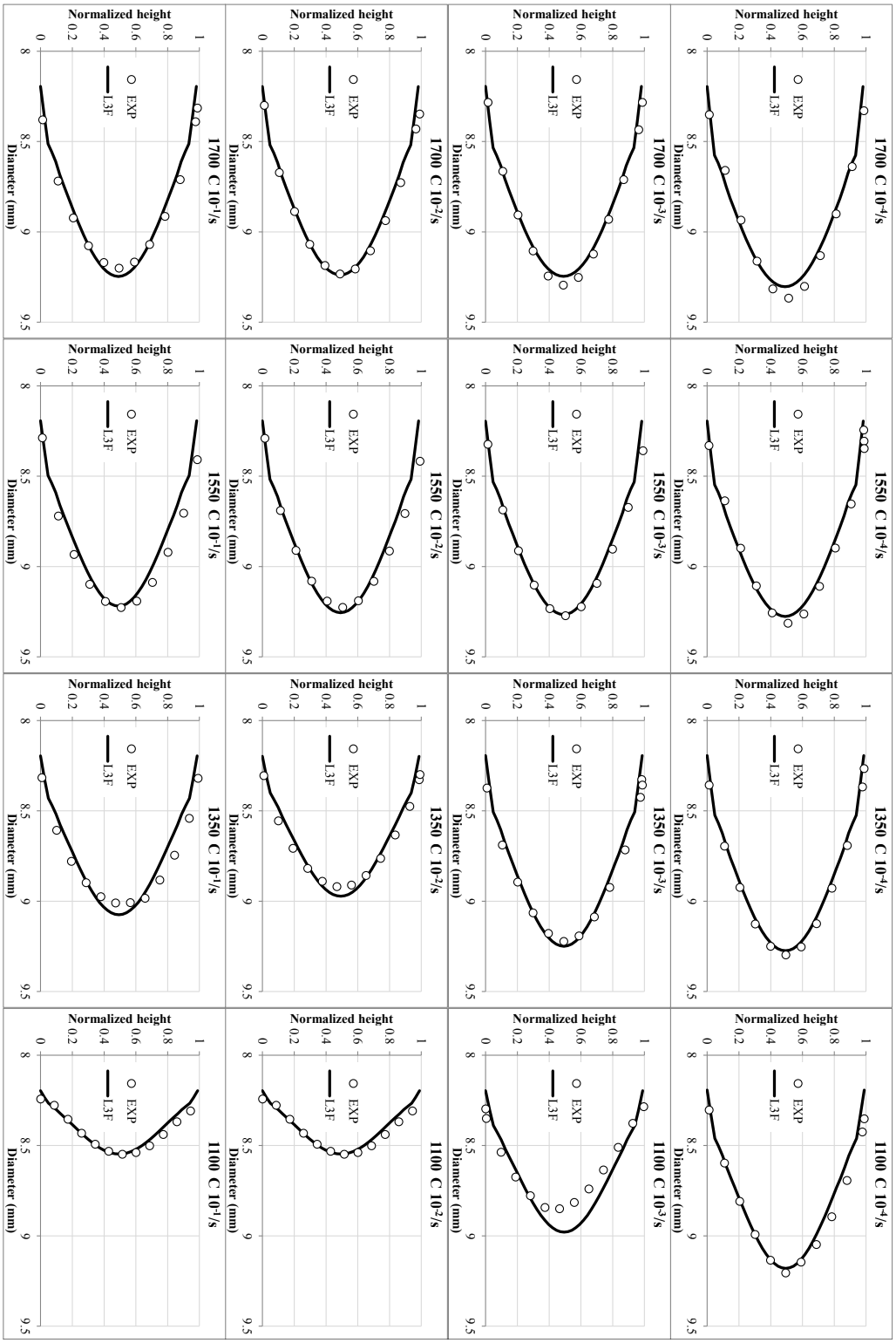

Figure 15: Calculated (L3F) and measured (EXP) diameter axial profiles after all the tests.

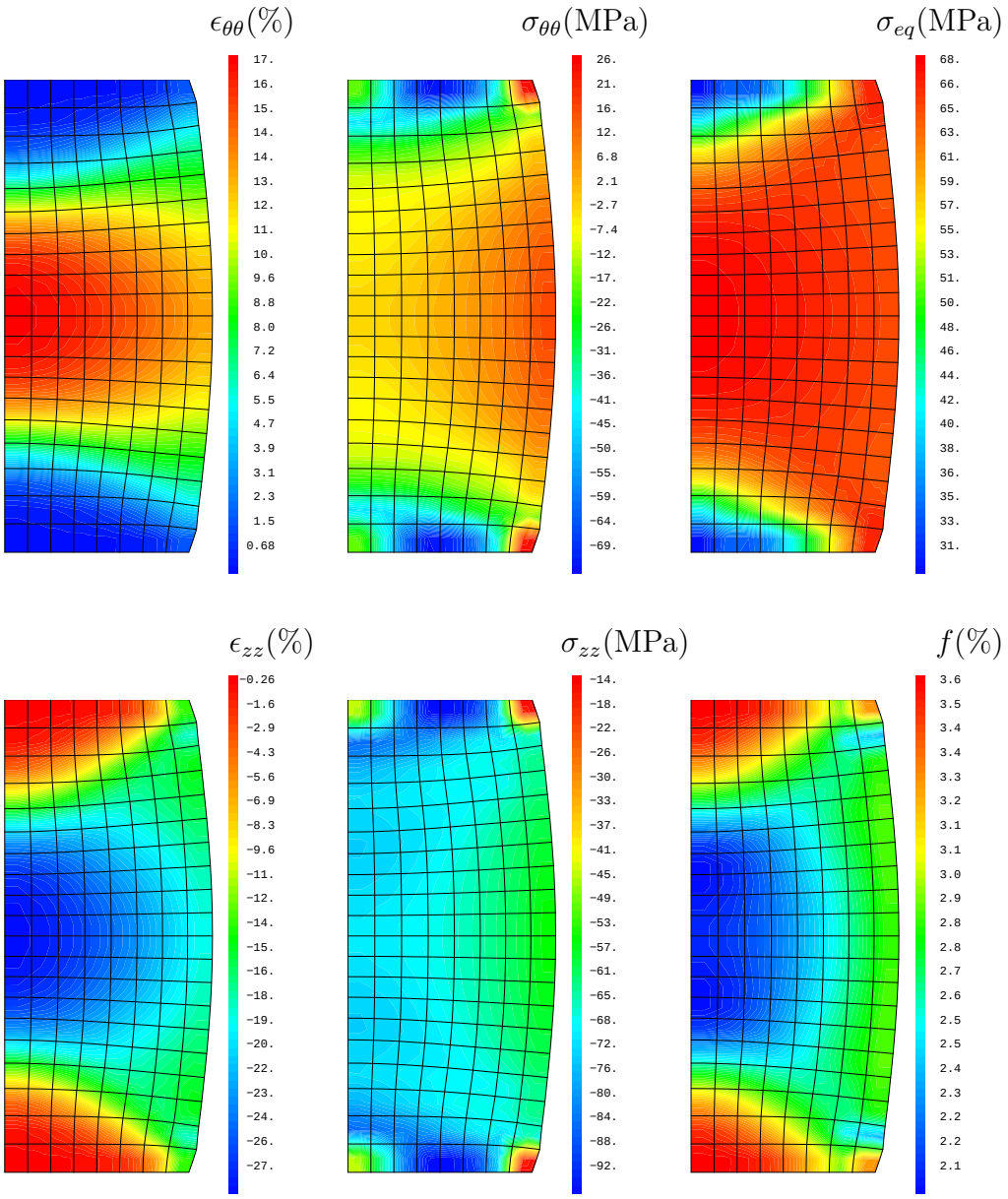

Figure 16: Isovalues of hoop and axial strains, hoop and axial stresses, second stress invariant and porosity in the pellet tested at 1700°C and 10^{-3}/s.

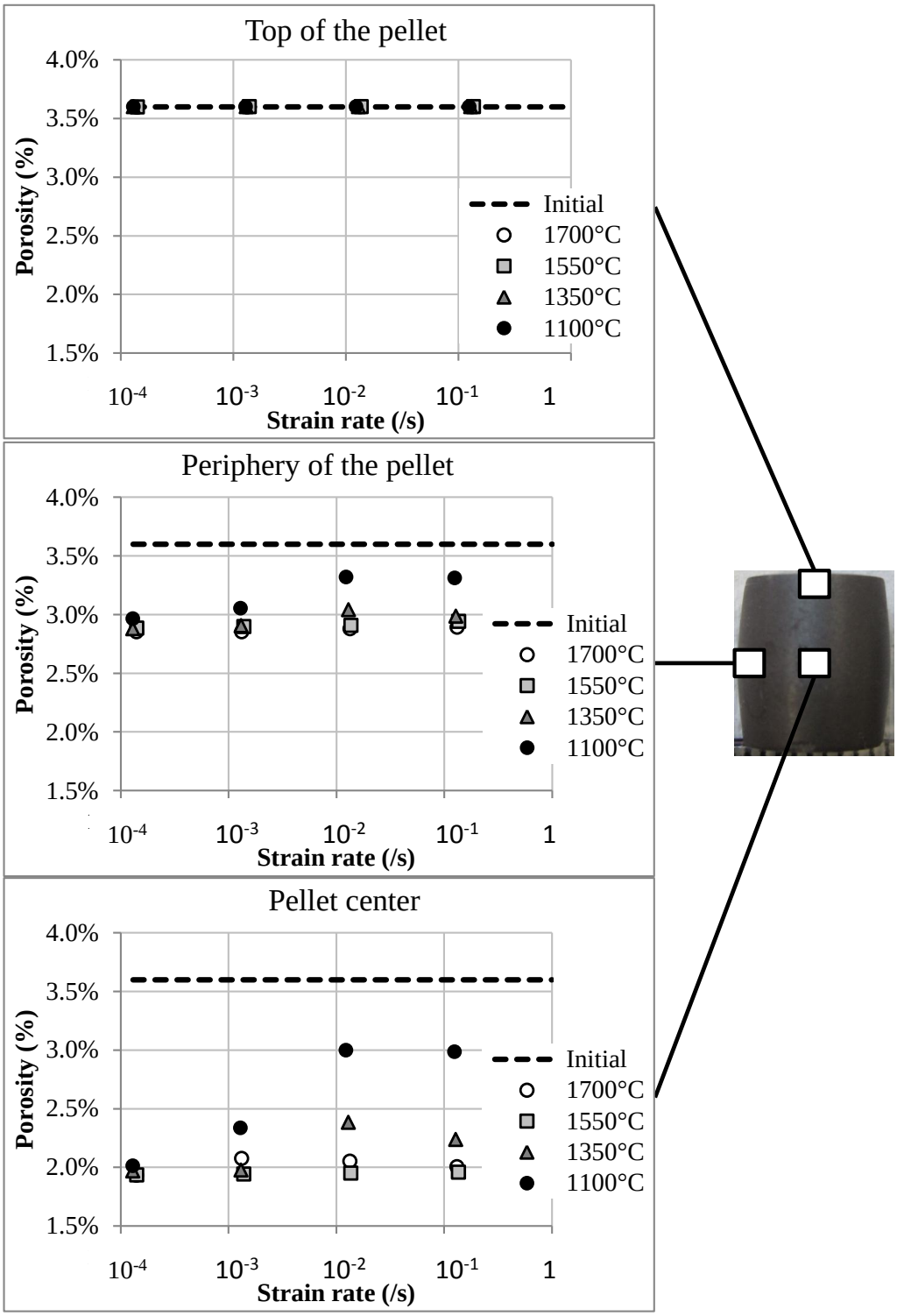

Figure 17: Calculated porosities after the tests at the top, center and periphery of the samples.

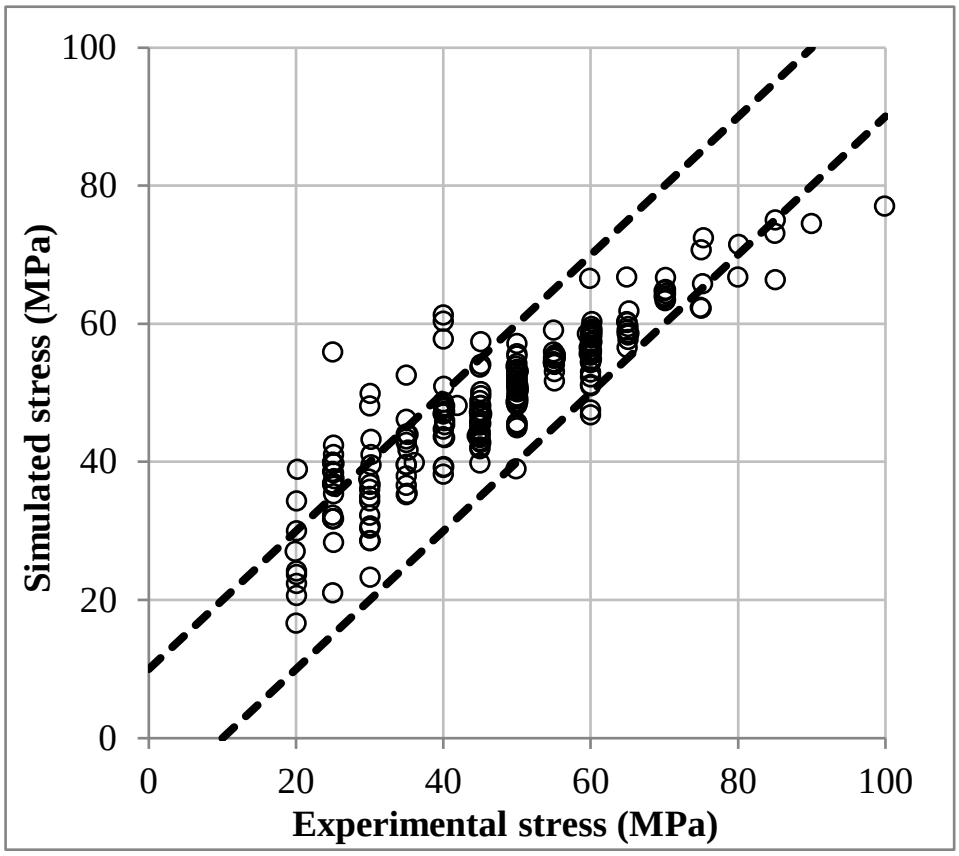

Figure 18: Calculated and measured creep stresses in 231 creep tests.